Carbohydrate Polymers 324 (2024) 121536

Contents lists available at ScienceDirect

Carbohydrate Polymers

journal homepage: www.elsevier.com/locate/carbpol

Vancomycin-loaded methylcellulose aerogel scaffolds for advanced bone tissue engineering

Ana Iglesias-Mejuto [a], Beatriz Magariños [b], Tânia Ferreira-Gonçalves [c,d], Ricardo Starbird-Pérez [e,f], Carmen Álvarez-Lorenzo [a], Catarina Pinto Reis [c,d], Inés Ardao [g], Carlos A. García-González [a,*]

[a] AerogelsLab, I+D Farma Group (GI-1645), Department of Pharmacology, Pharmacy and Pharmaceutical Technology, Faculty of Pharmacy, iMATUS and Health Research Institute of Santiago de Compostela (IDIS), Universidade de Santiago de Compostela, E-15782 Santiago de Compostela, Spain
[b] Departamento de Microbiología y Parasitología, Facultad de Biología, CIBUS, Universidade de Santiago de Compostela, E-15782 Santiago de Compostela, Spain
[c] Research Institute for Medicines (iMed.ULisboa), Faculty of Pharmacy, Universidade de Lisboa, Av. Professor Gama Pinto, 1649-003 Lisboa, Portugal
[d] Instituto de Biofísica e Engenharia Biomédica (IBEB), Faculdade de Ciências, Universidade de Lisboa, Campo Grande, 1749-016 Lisboa, Portugal
[e] Centro de Investigación y de Servicios Químicos y Microbiológicos (CEQIATEC), School of Chemistry, Instituto Tecnológico de Costa Rica, 159-7050 Cartago, Costa Rica
[f] Centro de Investigación en Ciencia e Ingeniería de Materiales (CICIMA), Universidad de Costa Rica, 11501-2060 San José, Costa Rica
[g] BioFarma Research group, Department of Pharmacology, Pharmacy and Pharmaceutical Technology, Innopharma Drug Screening and Pharmacogenomics Platform, Centro Singular de Investigación en Medicina Molecular y Enfermedades Crónicas (CiMUS), Universidade de Santiago de Compostela, E-15782 Santiago de Compostela, Spain

ARTICLE INFO

Keywords:
3D-printing
Aerogels
Supercritical sterilization
Vancomycin

ABSTRACT

Scaffolds grafting combined with local delivery of antibiotics at the injury site may promote bone regeneration along with prevention of infections. In this work, a processing strategy combining the 3D-printing of polysaccharide-based inks with supercritical (sc)CO_2 technology was employed to manufacture drug-loaded, nanostructured, and personalized-to-patient aerogels for the first time. Methylcellulose (MC) was employed as graft matrix endowed with nanohydroxyapatite (nHA) to confer bioactivity as required in bone tissue engineering (BTE). MC-nHA aerogels were obtained through the 3D-printing of hydrogel-based scaffolds followed by $scCO_2$ drying. Aerogels were loaded with vancomycin (VAN), an antibiotic employed in the management of bone infections. Textural properties and printing fidelity of scaffolds were studied as well as VAN release, long-term bioactivity, and pre-osteoblasts mineralization. In vitro cell studies and in vivo *Artemia salina* tests were carried out to evaluate the potential toxicity of the antibiotic-loaded aerogels. Aerogels efficacy in inhibiting bacterial growth was assessed by antimicrobial tests with *Staphylococcus aureus*. Textural stability of the aerogels after 7 months of storage was also evaluated. Obtained results showed that the scaffolds promoted the intended two-in-one effect (bone repair and infection management simultaneously) in a personalized way, regulating formulation design, drug dose, and porosity.

1. Introduction

The incidence of bone lesions due to falls and traffic accidents is increasing with the progressive ageing of the population as major cause. Patients usually present open wounds and bone defects, commonly accompanied with the activation of infection and inflammation molecular pathways, that significantly hamper the natural healing process (Spellberg & Lipsky, 2012). Furthermore, implant-associated post-operative and post-traumatic bone infections commonly come up with antibiotics side effects, hospitalization, and the subsequent health economics costs (Trampuz & Zimmerli, 2008). *S. aureus* is the most prevalent microorganism leading to graft-associated bone infections (Gallarate et al., 2021). Debridement and intravenous administration of antibiotics is the conventional treatment for open bone injuries with important drawbacks, like the low antibiotic concentration at the wound site that can promote the development of methicillin-resistant *S. aureus* (MRSA) resulting in repeated bacterial infections (Barakat et al., 2019; Poeppl et al., 2014). Vancomycin (VAN) is the only antibiotic sensitive

* Corresponding author.
E-mail address: carlos.garcia@usc.es (C.A. García-González).

https://doi.org/10.1016/j.carbpol.2023.121536
Received 1 August 2023; Received in revised form 20 October 2023; Accepted 27 October 2023
Available online 4 November 2023

to MRSA and effective in inhibiting inflammatory reactions in bone infections (Lv et al., 2022). Advanced on-site delivery systems of VAN are required for an effective treatment of orthopaedical surgery-related bone infections, avoiding or reducing VAN side effects.

Three-dimensional (3D) printing is a simple and versatile manufacturing technology that enables the production of intricate and multicomponent grafts employed as provisional supports for new tissue formation (Shin et al., 2020). Different 3D-printing strategies have been used in different biomedical fields (Jiang et al., 2021). Specifically, extrusion-based 3D-printing is the most widely employed for tissue scaffolding (Derakhshanfar et al., 2018), allowing the generation of well-organized, and hierarchical tissue equivalents composed by polymers, bioactive molecules and cells (Ahlfeld et al., 2020). Methylcellulose (MC) is a biocompatible and biodegradable cellulose derivative commonly used as 3D graft matrix (Ahlfeld et al., 2020; Shin et al., 2020). MC is a thermo-gelling polysaccharide with a fully reversible gelation in aqueous media.

Aerogels are low density and highly mesoporous materials intensively employed for medical (e.g., tissue scaffolds or drug delivery systems) and non-medical (e.g., water purification or thermal insulation) applications (Tetik et al., 2021; Yahya et al., 2021). They are obtained from wet gels by processing techniques (typically, $scCO_2$ drying) able to replace the liquid inside these gel networks with a gas under mild operating conditions (García-González et al., 2021). Particularly, the outstanding structural performance of aerogels and the excellent biological behavior of polysaccharides (biocompatibility, biodegradability) unveiled polysaccharide aerogels as promising candidates for the development of advanced tissue engineering scaffolds for regenerative medicine (Bernardes et al., 2021; Iglesias-Mejuto & García-González, 2021; Ng et al., 2022). Moreover, the recently proposed dual processing strategy combining 3D printing and $scCO_2$ drying leads to personalized aerogels with dual porosity adequate for BTE (Iglesias-Mejuto & García-González, 2021, 2022).

New formulations for an efficient delivery of VAN triggered by implantation to reach and maintain antibiotic therapeutic levels in the injury site, while promoting long-term osseointegration and ensuring biocompatibility are needed for the treatment of infections associated to bone defects. In this work, 3D-printed and VAN-loaded polysaccharide aerogels were manufactured for the first time with a personalized shape and drug content and specifically evaluated for simultaneous bone tissue engineering (BTE) and infection management. Aerogels were loaded with nanohydroxyapatite (nHA), a common bone repair component with good osteoconduction and osteoinduction (Kohyama et al., 2018). $scCO_2$ drying was performed to obtain the drug-loaded aerogels. The textural characteristics of the aerogels were obtained by BET and SEM analyses, the printing fidelity was evaluated with respect to the original design and their mechanical performance was assessed by dynamic mechanical analysis (DMA). Bioactivity of aerogels was tested by immersion in simulated body fluid (SBF), biocompatibility and mineralization by cellular assays, hemocompatibility by Hen's egg test on the chorioallantoic membrane (HET-CAM) tests and their safety by *A. salina* assays. Microbiological tests against *S. aureus*, loading efficiency, entrapment yield and VAN release tests were also carried out. A spatial personalization in the drug dose (with two different VAN contents in one structure) and in the morphology of the aerogels were achieved for the first time by the dual processing strategy herein used. 3D-printed aerogels exhibited a sustained VAN release profile essential for bone infection management as well as the long-term bioactivity required for BTE applications.

2. Materials and methods

2.1. Materials

MC (viscosity: 15 cP), nHA (M_w: 502.31 g/mol, purity ≥97 %), alizarin red and cetylpyridinium chloride were provided by Sigma-Aldrich (Steinheim, Germany). Hydroxyapatite (HA, M_w 502.31 g/mol, reagent grade purity, micropowder) was supplied by Fluidinova (Moreira da Maia, Portugal). VAN hydrochloride (M_w: 486.0 g/mol, purity: 94.3 %) was provided by Guinama (La Pobla de Vallbona, Spain). CO_2 (purity >99.9 %) was supplied by Nippon Gases (Madrid, Spain) and absolute ethanol (EtOH) by VWR (Radnor, PA, USA). Water was purified by reverse osmosis (resistivity >18 MΩ·cm; Milli-Q, Millipore®, Madrid, Spain).

2.2. 3D-printing of hydrogels

Milli-Q water was used as solvent to prepare aqueous inks. Different concentrations of MC (12, 15, 18 and 20 wt%), nHA/HA (0, 6, 12 and 24 wt%) and/or VAN (0, 5, 10 and 15 wt%) with respect to water were employed. MC solutions were firstly prepared, and nHA/HA and/or VAN were then added. Inks were prepared under vigorous agitation (600 rpm) employing a homogenizer (VWR vos 60, Radnor, PA, USA) for at least 1 h at room temperature (RT). They were degassed in a sonication bath (Branson 3510 Emerson, Ferguson, MO, USA) for 10 min to eliminate air bubbles prior to their use as inks for their rheological evaluation and subsequent 3D-printing.

3D-printed hydrogels were obtained with a Cellink BIOX Bioprinter (Boston, MA, USA) using an extrusion printhead at 40 °C, a 3-mL syringe and a 410-μm nozzle at a printing pressure of 40 kPa and a printing velocity of 3 mm/s. Hydrogel dimensions were 20x20x3 mm with a grid pattern and 8 layers. After the printing process, all scaffolds were put in contact with ethanol and alcogels were thus obtained.

2.3. Rheological evaluation of inks

Flow behavior of inks was recorded at 20 and 40 °C between 0.05 and 200 rad/s in a Rheolyst AR-1000 N rheometer (TA Instruments, Newcastle, UK) equipped with a Peltier plate and a cone geometry (40 mm diameter, 2°) with a solvent trap. For each formulation, at least four replicates were evaluated. The Eq. (1) (power law) was fitted to the linear region of the viscosity (η) vs shear rate (γ) curves.

$$\eta = b\gamma^{c} \tag{1}$$

where b and c are the consistency and flow indices, respectively.

2.4. $scCO_2$ drying of 3D-printed alcogels

Alcogels were placed into a 100-mL stainless steel autoclave (Thar Process, Pittsburg, PA, USA) and immersed in 25 mL of EtOH. A continuous CO_2 flow rate (5–7 g/min) at 120 bar was supplied for 4 h into the autoclave, maintained at 40 °C. After CO_2 depressurization to atmospheric pressure at a constant rate of 2 bar/min, aerogels were collected from the autoclave and stored at RT for further analysis. Aerogels obtained were described in Table 1 and denoted as MC *x* nHA (or HA) *y* VAN *z* (being $x = 12, 15, 18, 20$ wt%; $y = 6, 12, 24$ wt%; $z = 5, 10, 15, 5/15$ wt%- 5 and 15 wt% in alternative layers-). When the formulation contained MC and nHA/HA/VAN, the MC percentage was set always to 12 wt% and simply denoted as "MC" (i.e. without *x*).

2.5. Physicochemical characterization of 3D-printed aerogels

Skeletal density of aerogels (ρ_{skel}) was measured at RT with a helium pycnometer (Quantachrome, Boynton Beach, FL, USA) at the pressure of 1.01 bar. Values were obtained from five replicates. Apparent density (ρ_{app}) was calculated from Eq. (2), and scaffold porosity (ε) was determined according to Eq. (3):

$$\rho_{app} = \text{aerogel mass} / \text{aerogel volume} \tag{2}$$

$$\varepsilon\ (\%) = \left[1 - \left(\rho_{app}/\rho_{skel}\right)\right] \times 100 \tag{3}$$

Table 1
MC aerogel formulations studied.

Aerogel scaffold	Ink composition			
	MC (wt %)	HA (wt %)	nHA (wt %)	VAN (wt%)
MC	12	–	–	–
MC 15	15	–	–	–
MC 18	18	–	–	–
MC 20	20	–	–	–
MC HA 6	12	6	–	–
MC HA 12	12	12	–	–
MC HA 24	12	24	–	–
MC nHA 6	12	–	6	–
MC nHA 12	12	–	12	–
MC nHA 24	12	–	24	–
MC VAN 5	12	–	–	5
MC VAN 10	12	–	–	10
MC VAN 15	12	–	–	15
MC nHA 24 VAN 10	12	–	24	10
MC VAN 5/15	12	–	–	5 (4 layers); 15 (4 layers)

External dimensions of scaffolds were measured to determine step and overall volume shrinkages following Eqs. (4) and (5), respectively:

$$\text{Step volume shrinkage}\ (\%) = [(\text{Alcogel volume} - \text{Aerogel volume})/\text{Alcogel volume}] \times 100 \quad (4)$$

$$\text{Overall volume shrinkage}\ (\%) = [(\text{Hydrogel volume} - \text{Aerogel volume})/\text{Hydrogel volume}] \times 100 \quad (5)$$

Low-temperature N_2 adsorption-desorption analysis (ASAP 2000 Micromeritics Inc.; Norcross, GA, USA) was employed to evaluate aerogels' textural parameters. Samples were degassed under vacuum at RT for 24 h before being analyzed. Specific surface area (A_{BET}) of aerogels was obtained applying the BET (Brunauer–Emmett–Teller) method. Specific pore volume (V_p), pore size distribution and mean pore diameter (d_p) were calculated by using the BJH (Barrett–Joyner–Halenda) method. Morphology of aerogels was assessed by scanning electron microscopy (SEM, EVO LS15, Zeiss, Oberkochen, Germany). Samples were iridium-sputtered before being imaged to improve image quality by decreasing charging. 7-month textural stability tests of the most promising formulation (MC nHA 24 VAN 10) and MC aerogels (control) were also performed by N_2 adsorption–desorption and SEM studies after storage of the aerogels in closed plastic jars, at RT and protected from light.

Attenuated Total Reflectance/Fourier-Transform Infrared Spectroscopy (ATR-FTIR) was performed with a Gladi-ATR accessory using a diamond crystal (Pike, Madison, WI, USA) to evaluate the chemical structure and confirm the presence of all components on the end structures. Raw materials and aerogels were characterized in the mid-IR spectrum range (400–4000 cm^{-1}) using 32 scans and at a resolution of 2 cm^{-1}. X-ray diffraction (XRD, PW-1710, Philips, Eindhoven, The Netherlands) was used to test possible physical modifications in aerogels when VAN was incorporated. Diffractograms were collected in the 2–50° (2θ-range) using a 0.02° step and CuKα$_1$ radiation.

2.6. Printing fidelity tests

Shape fidelity factor (SFF) index was employed to assess the fidelity of hydrogels, alcogels and aerogels with respect to the original printing file. SFF was calculated from Eq. (6):

$$SFF = A_i/A \quad (6)$$

where A_i is the hydrogel, alcogel or aerogel printed area, and A is the computer aided design (CAD) area, as defined in the printing file.

2.7. Mechanical evaluation by DMA

Storage modulus (E′), loss modulus (E″), and damping ratio (tan δ = E″/E′) of 3D-printed biocomposites were measured at RT. Compression tests were performed using a DMA RSA-G2 equipment (TA Instruments, Waters, New Castle, DE, USA) with a 5 mm compression geometry. A 0.01 N pre-load was applied to ensure contact between the samples and the adapted parallel plates at a strain value of 0.5 % and from 0.1 to 50 Hz as frequency range. At least three measurements were performed for each formulation.

2.8. Bioactivity tests

SBF medium was prepared with ion concentrations nearly equal to those of human plasma and adjusted to pH 7.4 (Kokubo & Takadama, 2006). Aerogels were cut into 1 × 1 × 0.3 cm samples, placed into plastic conical tubes and immersed in 35 mL of SBF at 37 °C to evaluate aerogels bioactivity. After 13 and 26 days, wet gels were immediately rinsed three times with deionized water and dried by lyophilization. Bioactivity was assessed by SEM and EDX focusing on surface mineral depositions (Duarte et al., 2009).

2.9. VAN loading and entrapment yield on aerogels

VAN entrapment yield was assessed by immersing VAN-loaded aerogels of known dimensions (1 × 1 × 0.3 cm) and weight (ca. 50 mg) in 25 mL of phosphate buffer saline (PBS) pH 7.4. Samples were kept under magnetic stirring (1000 rpm) until being completely dissolved. Obtained solutions were measured by UV/Vis spectroscopy (8453, Agilent, Santa Clara, CA, USA) at a wavelength of 281 nm. Tests were carried out in triplicate and aerogels without VAN were also tested to eliminate the interference of MC or nHA in UV/Vis measurements. VAN loading and entrapment yield were obtained from Eqs. (7) and (8), respectively.

$$\text{Drug } loading\ (\%) = \left(W_p/W_{aer}\right) \times 100 \quad (7)$$

$$\text{Drug entrapment } yield\ (\%) = \left(W_p/W_t\right) \times 100 \quad (8)$$

where W_p is the VAN amount in aerogels measured by UV/Vis analysis, W_{aer} is the total weight of aerogels, and W_t is the initial VAN amount added for aerogels preparation. VAN calibration curve in PBS pH 7.4 medium was obtained and validated in the 0.05–0.22 mg/mL range ($R^2 > 0.99$).

2.10. VAN release tests from aerogels

VAN-loaded aerogels of known weight (ca. 20 mg) were placed into plastic conical tubes with 25 mL of PBS pH 7.4. Samples were put into an oscillating bath (P Selecta Unitronic 320 OR, Barcelona, Spain) at 37 °C and 100 rpm for 72 h. 1-mL aliquots of medium were sampled at selected times (0, 0.25, 0.5, 1, 2, 4, 8, 24, 48 and 72 h), measured by UV/Vis

spectroscopy at the wavelength of 281 nm (8453, Agilent, Santa Clara, CA, USA), and replaced with 1 mL of fresh PBS. VAN release profiles were fitted to the first-order release pharmacokinetic model according to Eq. (9).

$$\%\text{VAN released} = 100 \text{ x } \left(1\text{–}e^{-kt}\right) \quad (9)$$

where k is the kinetic coefficient and t is the elapsed release time.

2.11. Cell viability and mineralization tests

Cytocompatibility of 3D-printed aerogels was determined by assessing the viability of mouse embryo fibroblasts (NIH/3T3) after 24 and 72 h of culture in the presence of aerogels employing a resazurin assay, based on mitochondrial activity of living cells. Fibroblasts (2000 cells/cm^2) were seeded in 24-well plates containing 600 μL of Dulbecco's Modified Eagle's Medium growth media supplemented with 10 % bovine calf serum, penicillin 100 U/mL and streptomycin 100 g/mL and were incubated at 37 °C in a humidified atmosphere enriched with 5 % CO_2. Aerogels (0.5 × 0.5 × 0.3 cm) were UV-sterilized for 30 min and then placed in the wells with cells using culture inserts. Positive controls of cells without aerogels exposure were maintained at the same conditions and all tests were performed in triplicate. After 24 and 72 h of culture, aerogels were removed, growth medium was aspirated and 100 μL of 44 μM resazurin in growth medium was added into each well. Resazurin solution alone was tested as blank. After 3 h incubation under same conditions, fluorescence was measured at an excitation wavelength of 544 nm and emission wavelength of 590 nm in a microplate reader (Infinite® M200, Tecan Group Ltd., Männedorf, Switzerland).

MC3T3-E1 pre-osteoblastic cells were also employed to perform alizarin red staining test. Cells were incubated at 37 °C in a humidified atmosphere enriched with 5 % CO_2 and cultured with alpha minimum essential medium supplemented with 10 % fetal bovine calf serum, penicillin 100 U/mL and streptomycin 100 g/mL, at a cell density of 1 × 10^5 cells/well in 12-well plates. After 24 h of culture, 3D-printed aerogels (0.5 × 0.5 × 0.3 cm) were UV-sterilized for 30 min and then placed in the wells with cells using culture inserts. Experiments were carried out in triplicate for each formulation tested. Osteogenic medium was prepared by the addition of 50 μg/mL ascorbic acid, 10 mM glycerophosphate, and 100 nM dexamethasone to the previous medium, added to pre-osteoblastic cells and subsequently replaced every 2–3 days. After 14, 21 and 28 days, cells were washed 3 times with PBS to remove cells debris and fixed with EtOH at 4 °C for 1 h. Cells were then washed twice with water and stained with 40 mM alizarin red (pH 4.2) by incubating at RT for 10 min. Cells were washed once with water and three times with PBS and optical microscopy images were taken in the wet and dry states using Operetta CLS equipment (PerkinElmer, Waltham, MA, USA). Residual stain was removed with 10 % cetylpyridinium chloride for 15 min and, after shaking plates moderately, the absorbance was measured at 562 nm using a microplate reader (Infinite® M200, Tecan Group Ltd., Männedorf, Switzerland).

2.12. Safety tests using A. salina model

All in vivo studies were conducted in accordance with the European regulation (Directive 2010/63/EU) on care and use of animals in experimental procedures and the ARRIVE guidelines. Experiments were reviewed and approved by the Animal Experiment Ethics Committee (ORBEA) of the Faculty of Pharmacy of the University of Lisbon. Safety of VAN-loaded aerogels was evaluated by measuring the mortality of *A. salina* after 24 h of contact with aerogels as a preliminary in vivo model (Ferreira-Gonçalves et al., 2022; Hamidi et al., 2014). Commercial sea water salt was dissolved in tap water according to the instructions of the supplier. *A. salina* eggs were left to hatch in that solution at 25–30 °C for 48 h, under aeration and illumination. 1 mL of sea water with 10–15 nauplii was transferred to individual wells of a 24-well plate and aerogels (0.5 × 0.5 × 0.3 cm) were also added to wells using six replicates per formulation. 100 μL of artificial sea water and 100 μL of DMSO 100 % were used as negative and positive controls, respectively. Nauplii in contact with aerogels were incubated for 24 h under the same conditions and dead *A. salina* per well were counted. 100 μL of DMSO 100 % was added to kill the remaining alive nauplii after 24 h, total *A. salina* per well were counted and the mortality was then calculated according to Eq. (10).

$$\text{Mortality } (\%) = (\text{Dead 24 h}/\text{Dead Total}) \times 100 \quad (10)$$

where Dead 24 h is the number of dead nauplii after 24 h of contact with aerogels and Dead Total is the total number of nauplii per well.

2.13. HET-CAM tests

VAN-loaded aerogels were evaluated by HET-CAM tests according to Interagency Coordinating Committee on the Validation of Alternative Methods (ICCVAM) guidelines (Recommended Test Method Protocol: Hen's Egg Test – Chorioallantoic Membrane (HET-CAM) Test Method, 2010; Salerno et al., 2017). Tests were carried out using fresh and fertilized hens' eggs (50–60 g, Coren, Ourense, Spain) after horizontal incubation in a climatic chamber (Ineltec CC SR 0150, Barcelona, Spain) at 37 °C and 60 % humidified atmosphere with an 8-h scheduled rotation. On day 9, a small window was open in the eggshell with a scalpel to access the CAM. 300 μL of 0.1 N NaOH and 0.9 % NaCl were put in contact with CAM as positive and negative controls, respectively. Aerogels were also put in contact with CAM and each test was carried out in triplicate. Vessels of CAM were observed for 5 min to evaluate the appearance of hemorrhage (vessels bleeding), vascular lysis (vessels disintegration), clotting (denaturalization of intra and extravascular proteins), hyperemia (increase of blood flow) or changes in small vessels diameter of CAM by visual inspection and compared to controls.

2.14. Antimicrobial tests of 3D-printed aerogels

Sterile VAN-loaded aerogels were put in contact with a susceptible strain of *S. aureus* (ATCC 25923) previously seeded in a tryptic soy agar (TSA) plate for inhibition zone (halo) evaluation after 24 h of incubation at 37 °C. Same procedure was performed using tryptocasein soy broth (TSB) tubes (*S. aureus* concentration: 6 × 10^8 colony forming units per mL -CFU/mL-). Sterile aerogels without VAN were used as controls.

2.15. scCO$_2$ sterilization of 3D-printed aerogels

Aerogels were introduced into thermally sealed sterilization pouches and placed in a high-pressure 600-mL autoclave (NovaGenesis, NovaSterilis Inc., Ithaca, NY, USA) at 40 °C. 1200 ppm of H_2O_2 were loaded into the autoclave before being pressurized with CO_2 until 100 bar. After 30 min of contact time, the system was depressurized at a constant flow rate of 5 bar/min until atmospheric pressure. Sterilization efficacy was confirmed by seeding the thus sterilized aerogels in a TSA plate and in TSB tubes for CFU quantification, at 37 °C for 24 h. Textural properties of the sterilized aerogels were compared with the corresponding untreated formulations.

2.16. Statistical analysis

Results were reported as mean value ± standard deviation and post hoc Tukey HSD multiple comparison tests were carried out to determine the statistical significance of the differences among groups and the concerning controls. Values of $p < 0.05$ were considered as statistically significant.

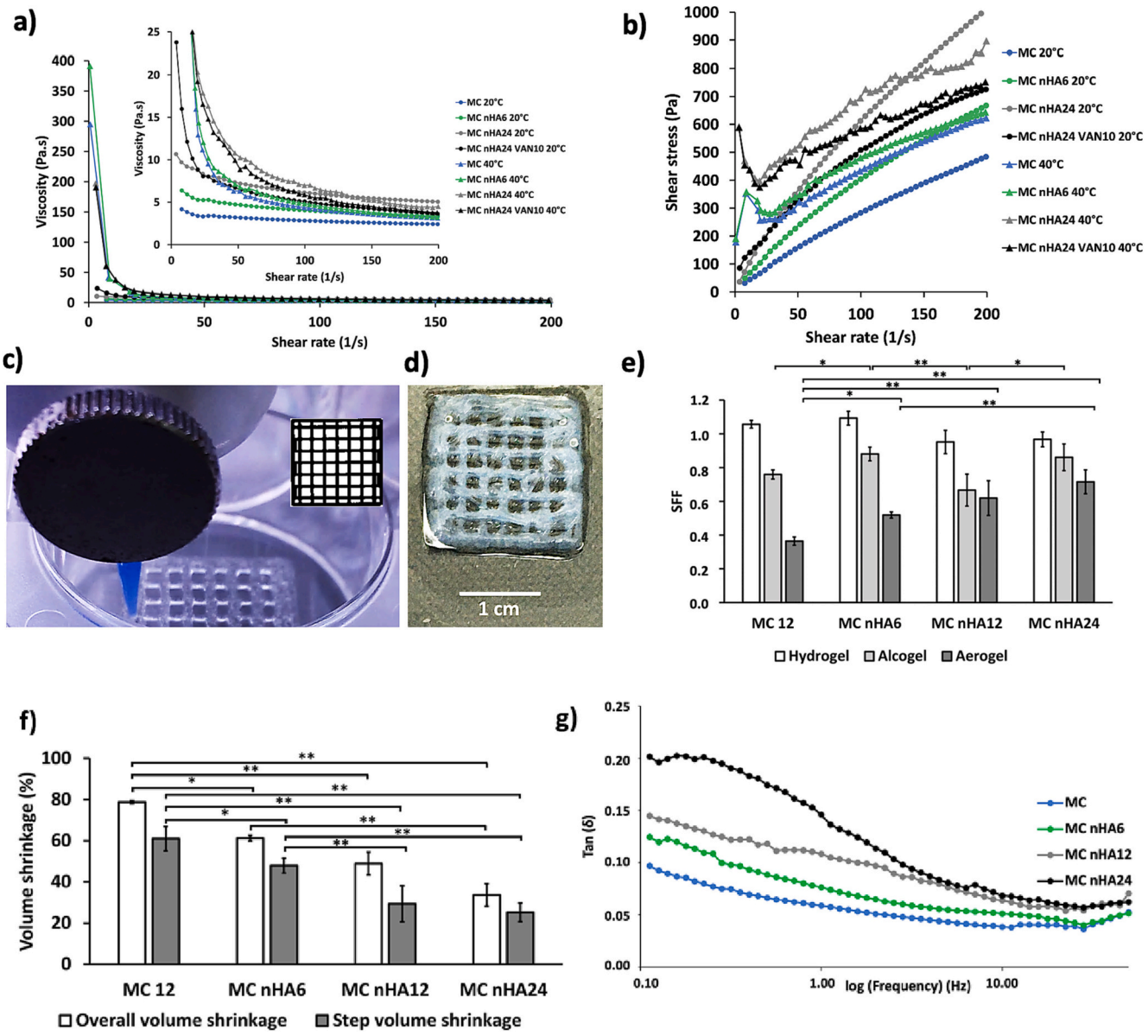

Fig. 1. Rheological evaluation of different ink formulations by (a) overall viscosity variation with respect to the shear rate and (b) shear stress with respect to shear rate. (c) MC hydrogel scaffolds during the 3D-printing process, CAD printing file (intake in c), and (d) MC gel scaffolds after solvent exchange to ethanol. (e) SFF index of MC hydrogel, alcogel and aerogels. (f) Overall and step volume shrinkage of MC aerogels. (g) DMA frequency sweep of tan δ for aerogels with increasing nHA content. Significant differences among groups were represented as * or ** (post hoc Tukey HSD multiple comparison test, $p < 0.05$ or $p < 0.01$, respectively).

3. Results and discussion

3.1. Rheological evaluation of inks

MC inks were homogeneously manufactured with different concentrations of nHA and/or VAN and the 3D-printing was performed without relevant clogging for all the studied formulations (Table 1). Extrusion-based 3D-printing process was simulated by analyzing the viscosity of the inks with respect to the shear rate (Corker et al., 2019). Flow tests of the inks demonstrated the shear-thinning behavior at low shear-stress conditions (Fig. 1a), which should facilitate the extrusion during the 3D-printing at moderate pressures. Shear thinning properties are essential to promote 3D-printing fidelity and a homogeneous distribution of the drug in the end structures. All formulations reached higher viscosities at 40 °C than at 20 °C, which is coherent with the thermal-responsiveness behavior of MC (Cochis et al., 2018; Shin et al., 2020). Moreover, a non-linear relation between shear stress and shear rate was observed for all formulations (Fig. 1b), thus suggesting a pseudoplastic behavior.

All rheological measurements were fitted to the power law equation (Eq. (1)). *b* values suggest higher extrudability at 20 °C (Table 2), probably due to the lower viscosities reached by MC at lower temperatures (Fig. 1a). *c* values obtained were closer to 0 when the rheology tests were performed at 40 °C (Table 2), indicating a more pronounced

Table 2
Shear thinning coefficient values of inks calculated through power law model.

Aerogel formulations	20 °C		40 °C	
	b	c	b	c
MC	6.95	0.80	61.74	0.43
MC nHA 6	12.19	0.76	85.85	0.38
MC nHA 24	19.86	0.74	203.80	0.27
MC nHA 24 VAN 10	33.96	0.58	223.50	0.22

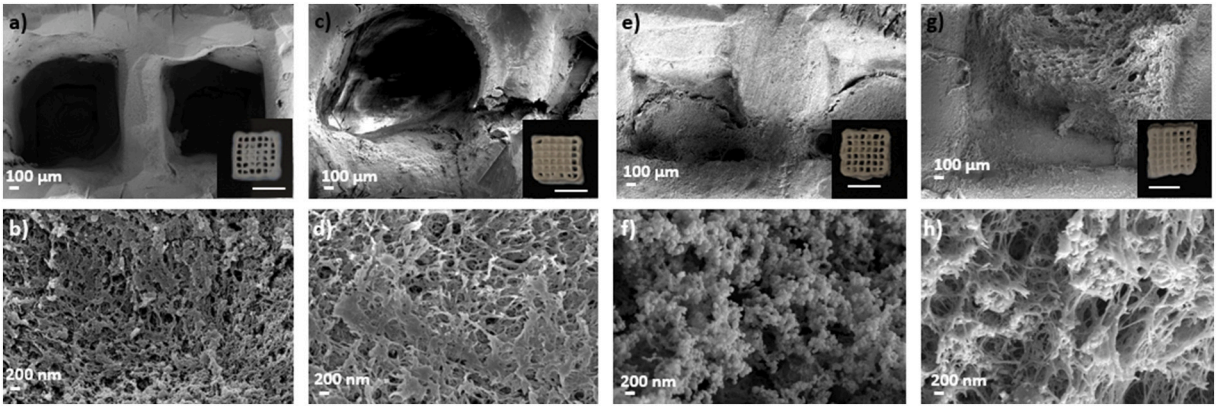

Fig. 2. SEM images of MC nHA-loaded aerogels: (a,b) MC 12; (c,d) MC nHA 6; (e,f) MC nHA 12; (g,h) MC nHA 24. Intake in a,c,e,g: Visual appearance of the 3D-pattern of aerogels (scale bar: 1 cm).

Table 3
Textural properties of MC nHA-loaded aerogels.

Aerogel scaffold	A_{BET} (m^2/g)	d_p (nm)	V_p (cm^3/g)	ρ_{app} (g/mL)	ρ_{skel} (g/cm^3)	ε (%)
MC	268 ± 13	19 ± 1	1.71 ± 0.09	0.18 ± 0.04	1.35 ± 0.03	87 ± 3
MC nHA 6	259 ± 13	24 ± 1	1.83 ± 0.09	0.22 ± 0.02	1.54 ± 0.04	86 ± 1
MC nHA 12	235 ± 12	23 ± 1	1.76 ± 0.09	0.31 ± 0.01	1.76 ± 0.02	83 ± 1
MC nHA 24	165 ± 8	24 ± 1	1.36 ± 0.07	0.32 ± 0.03	1.92 ± 0.02	83 ± 2

Notation: A_{BET}: specific BET surface area, d_p: BJH-mean pore diameter, V_p: BJH-specific pore volume, ρ_{app}: *apparent density,* ρ_{skel}: skeletal density and ε: porosity.

shear thinning behavior and a better suitability for extrusion-based 3D-printing.

3.2. Physicochemical characterization of 3D-printed aerogels

Highly mesoporous 3D-printed MC aerogel scaffolds were manufactured with different MC concentrations (12 to 20 wt%; Fig. 2a and Fig. S1). The high textural properties obtained in all cases confirmed that the filaments of the 3D-printed structure were highly mesoporous (Table 3 and Table S1). Similar textural parameters, porous morphology and distribution to those obtained for these filaments of the MC aerogels were also described for nanofibrous cellulose aerogels (Wang et al., 2020). MC concentration was set at 12 wt% for ulterior tests in combination with nHA/HA and/or VAN as the 3D-printing process was difficult (frequent clogging of the printhead upon printing) when higher MC concentrations were employed.

MC aerogels containing nHA showed good textural properties regardless of the nHA content (Table 3). nHA has been previously linked to higher specific surface areas, bioactivity and closer elasticity to the cortical bone with respect to HA, being able to address HA poor toughness and better repair bone defects (Chen et al., 2021). HA was incorporated into MC aerogels, i.e. alternatively to nHA, for the sake of textural properties comparison (Table S1 and Fig. S2). The addition of HA caused a dramatic decrease in A_{BET} proportional to HA content (Table S1), as previously reported for alginate-HA scaffolds (Iglesias-Mejuto & García-González, 2021). Nevertheless, the incorporation of nHA in MC aerogels did not cause such a sharp decline in textural properties (Table 3) resulting in MC nHA scaffolds with improved textural properties with respect to their MC HA counterparts. Moreover, macroscopical SEM images show an accuracy loss in the 3D-pattern when HA was employed (Fig. S2a,c,e) maybe due to the increase of the ink viscosity with the HA content. For all these reasons, nHA-loaded aerogels were selected for further physicochemical and biological characterizations as well as for VAN incorporation.

Aerogels porosity (83–87 %, Table 3) is higher than those reported for other cellulose aerogels (60–90 %) (Lin et al., 2015), maybe due to the presence of large macropores originated from the 3D-pattern design on the herein manufactured structures.

A highly porous and interconnected microstructure was observed by SEM imaging for all nHA-loaded aerogels with a rougher pore structure when higher nHA contents were incorporated with respect to lower nHA contents (Fig. 2b,d vs Fig. 2f,h). Similar findings were reported for cellulose aerogels (Chen et al., 2021) and for alginate-cellulose scaffolds loaded with different HA concentrations (Tohamy, Soliman, et al., 2018).

Direct solvent exchange to ethanol results in aerogels with low step and overall volume shrinkages (Fig. 1f). Aerogels with the highest nHA content present the lowest step and overall volume shrinkages, with statistically significant differences with respect to the other formulations studied ($p < 0.01$). Higher volume shrinkages were reported for aerogels with lower nHA content, similar to those herein obtained for MC aerogels and also found for nanocellulose-based aerogels (50 %) (Zhang et al., 2021).

Good textural properties were found for VAN-loaded aerogels, with a slight increase in A_{BET} (Table 4). Highly interconnected and irregular pores with a dual size (mesopores and macropores) were found in nHA-VAN aerogels (Fig. 3b,d,f), suggesting that VAN incorporation did not induce relevant modifications in the porous structure of aerogels. An absence of relevant morphological changes due to VAN addition was also reported in chitosan-HA aerogels (Zhang et al., 2012). Finally, 3D-

Table 4
Textural properties of VAN-loaded polysaccharide aerogels.

Aerogel scaffold	A_{BET} (m^2/g)	d_p (nm)	V_p (cm^3/g)
MC VAN 5	376 ± 19	17.1 ± 0.8	2.20 ± 0.11
MC VAN 10	374 ± 19	23.3 ± 1.2	2.75 ± 0.14
MC VAN 15	326 ± 16	24.6 ± 1.2	2.68 ± 0.13
MC VAN 5/15	174 ± 9	19.3 ± 1.0	1.12 ± 0.06
MC nHA 6 VAN 10	254 ± 13	17.0 ± 0.8	1.46 ± 0.07
MC nHA 12 VAN 10	163 ± 8	21.7 ± 1.1	1.20 ± 0.06
MC nHA 24 VAN 10	106 ± 5	23.1 ± 1.2	0.82 ± 0.04
MC 12 st	170 ± 9	17.4 ± 0.9	1.04 ± 0.05
MC 12 nHA 6 st	139 ± 7	18.8 ± 0.9	0.89 ± 0.04
MC 12 nHA 12 st	192 ± 10	20.9 ± 1.0	1.33 ± 0.07
MC 12 nHA 24 st	227 ± 11	23.5 ± 1.2	1.78 ± 0.09
MC 12 S	213 ± 11	22.4 ± 1.1	1.59 ± 0.08
MC nHA 24 VAN 10 S	93 ± 5	20.8 ± 1.0	0.66 ± 0.03

Notation: st: $scCO_2$ sterilized aerogels, S: aerogels after 7 months of storage. A_{BET}: specific BET surface area, d_p: BJH-mean pore diameter, V_p: BJH-specific pore volume.

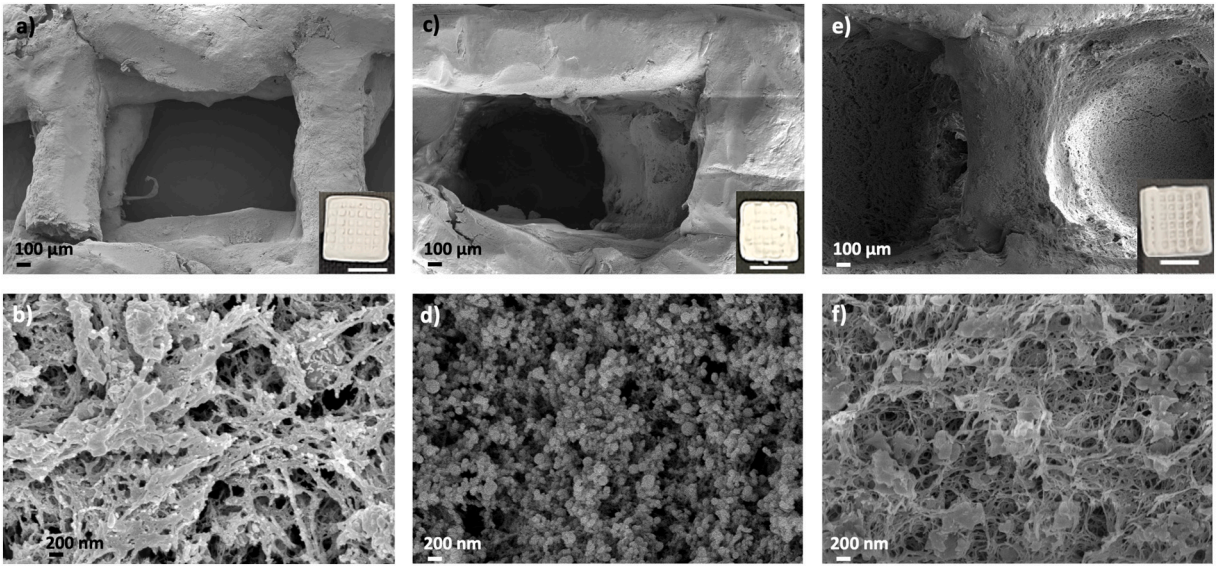

Fig. 3. SEM images of MC nHA-VAN aerogels: (a,b) MC nHA 6 VAN 10; (c,d) MC nHA 12 VAN 10; (e,f) MC nHA 24 VAN 10. Intake in a,c,e: Visual appearance of the 3D-pattern of aerogels (scale bar: 1 cm).

printed MC aerogels consisting of alternative layers containing two different VAN concentrations (5 and 15 wt%) were successfully manufactured (MC VAN 5/15) with a good textural performance. The low impact in the microstructure due to the customization of the drug content distribution within the scaffolds opens the possibility of developing specific gradient concentration profiles adapted to patient therapies necessities. Moreover, textural parameters after 7 months of storage had no relevant differences with respect to the same formulations evaluated just after their preparation (Table 4). SEM images still showed the dual porous structure essential for bone tissue engineering after storage in mild conditions (Fig. S3) and endorses the mid-term storage stability of MC and MC nHA 24 VAN 10 aerogels.

The XRD diffractograms of aerogels (Fig. S4a) exhibit its amorphous nature with two amorphous halos (7–15° and 15–25°) that could be attributed to the MC polymer network (Tohamy, Mabrouk, et al., 2018). Similar XRD patterns were obtained for MC and MC VAN 10 aerogels, suggesting that the amorphous structure of aerogels did not change due to VAN incorporation. ATR-FTIR spectroscopy was also performed to evaluate the effect of VAN incorporation on the chemical structure of aerogels. Interactions between aerogel components were observed in formulations loaded with VAN and/or nHA (Fig. S4b). Absorption bands detected at 3430 cm^{-1} and at 1631 cm^{-1} were assigned to hydroxyl groups and to H_2O, respectively, both present on nHA surface and previously described as essential for VAN bonding (Zhang et al., 2012). Absorption bands of the VAN are present on ATR-FTIR spectra at 3450, 1654, 1540 and 1230 cm^{-1} due to hydroxyl stretching, C═O stretching, C═C and phenol groups. These bands were in the spectra of VAN raw powder as well as on VAN-loaded 3D-printed aerogels, thus confirming the effective incorporation of VAN on aerogels. Finally, three specific nHA bands were clearly detected in the region close to 600 cm^{-1} of nHA raw powder and nHA-loaded aerogels, thus confirming the correct incorporation of nHA after all processing steps into the 3D-printed aerogels.

3.3. Printing fidelity evaluation

High printing fidelity was observed during the 3D-printing process (Fig. 1c) and after solvent exchange to ethanol (Fig. 1d). SFF is an index employed to assess the fidelity of 3D-printed structures with respect to the original CAD (Panraksa et al., 2020). The highest SFF values for aerogels were found at the highest nHA content ($p < 0.01$, Fig. 1e).

Table 5
E′, E″, and tan δ at 1 Hz for aerogels with increasing nHA content.

Aerogel scaffold	tan δ	E′ (MPa)	E″ (MPa)
MC 12	0.061 ± 0.002	7.8 ± 1.6	0.47 ± 0.09
MC nHA 6	0.089 ± 0.012	8.5 ± 2.7	0.75 ± 0.20
MC nHA 12	0.100 ± 0.009	13.2 ± 4.7	1.33 ± 0.52
MC nHA 24	0.131 ± 0.015	15.4 ± 3.2	2.06 ± 1.70

Lower SFF was observed in aerogels with respect to the corresponding alcogels precursors, as also described for alginate-HA scaffolds (Iglesias-Mejuto & García-González, 2021). Similar fidelity values were described for alginate-gelatin hydrogels, pointing out the high accuracy with respect to the CAD as well as the absence of a fidelity loss due to the solvent exchange (Giuseppe et al., 2018). Finally, SFF of MC nHA 24 alcogels is close to the described for cellulose hydrogels with similar cellulose content (12.5 %) but without nHA, thus indicating the lack of a negative impact on the printing fidelity due to nHA incorporation (Panraksa et al., 2020). These results further endorse the choice for nHA.

3.4. Mechanical analysis

The compressive modulus of the 3D-printed biocomposites was greatly influenced by its composition, displaying the best values with the highest nHA content in aerogels (Table 5). The internal friction between nHA and MC chains have previously resulted in the increment of E′ (Trakulsujaritchok & Hourston, 2006). A similar trend was observed after quantifying energy dissipation by damping measurements (Fig. 1g), phenomena occurring also in natural bone (Buechner & Lakes, 2003). Those data indicate a more elastic than viscous response with an increase in the inorganic content, tendency previously observed in the literature (Chen et al., 2019b; Kumar et al., 2014). It is important to note that natural bone is also a viscoelastic material with moduli depending on frequency, behavior also displayed by the aerogel formulations herein studied. Changes in bone damping factor are more relevant than changes in bone density as a consequence of strength because bone damping could attenuate locomotion impacts and it has been considered as indicative of integrity (Buechner & Lakes, 2003).

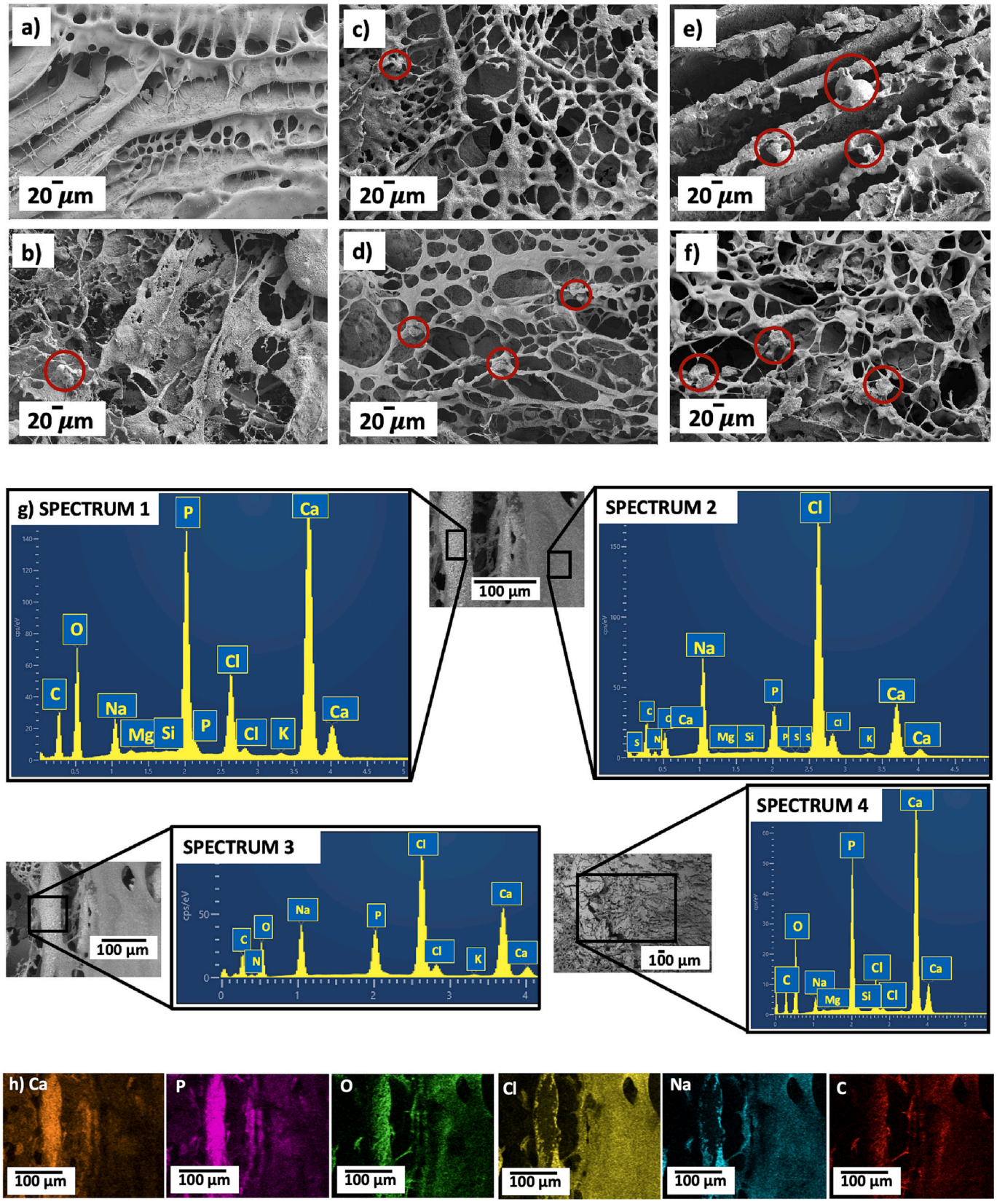

Fig. 4. (a) MC, (b) MC nHA 6, (c) MC nHA 12, and (d) MC nHA 24 aerogels after 13 days of bioactivity tests. (e) MC nHA 24 and (f) MC nHA 24 VAN 10 aerogels after 26 days of bioactivity tests. (g) EDX spectra of MC nHA 12 aerogels after 13 days in SBF in an apatite deposition zone (Spectrum 1), in a background zone (Spectrum 2), in general (Spectrum 3) and of MC nHA 24 VAN10 aerogels after 26 days in SBF (Spectrum 4). (h) EDX mapping of MC nHA 12 aerogels after 13 days in SBF. Red circles represent zones where the apatite depositions were detected by visual inspection.

3.5. Bioactivity assessment

After 13 days in SBF, a smooth porous surface was observed in MC aerogels (Fig. 4a), whereas small apatite depositions in the granular form were found dispersed only in the surface of nHA-loaded aerogels (Fig. 4b,c,d,e,f). The EDX spectrum of the granules presents marked peaks for Ca, P and O (Fig. 4g, Spectrum 1) confirming the presence of apatite depositions, while different peaks were detected in other regions of the same formulation (Na, Cl and Ca; Fig. 4g, Spectrum 2). The EDX spectrum for a wider region of nHA-loaded aerogels revealed peaks for Ca, P, O, Cl, K and Na (Fig. 4g, Spectrum 3), also described for alginate-cellulose scaffolds loaded with HA after SBF immersion (Tohamy, Soliman, et al., 2018). The EDX mapping of nHA-loaded aerogels (Fig. 4h) and the high Ca/P molar ratio suggest a good integrity and bonding between the organic and inorganic aerogel components, as well as the stimulation of bone tissue formation and functionality.

Apatite depositions found in nHA-loaded aerogels increased in size and number after 26 days (Fig. 4e,f; red circles). This apatite layer covering aerogel surface in a flower-like morphology in formulations loaded with nHA was previously described in MC nHA composites and was related to the presence of bone-like apatite (Drouet, 2013; Valarmathi & Sumathi, 2022). Change in intensity of Ca, P and O peaks (Fig. 4g, Spectrum 1) was very noticeable with respect to zones where apatite depositions were not found (i.e. without nHA) (Fig. 4g, Spectrum 2) endorsing that nHA presence clearly enhanced apatite formation. Aerogels exhibiting higher bioactivity (MC nHA24) were loaded with VAN for implement a strategy of advanced bone tissue engineering, combining bone infection treatment and tissue engineering simultaneously. MC nHA24 scaffolds show similar apatite depositions in number and size with (Fig. 4f) and without VAN (Fig. 4e) after immersion in SBF for 26 days. This finding indicates the absence of VAN interaction with the bioactivity process and suggests the suitability of this formulation for advanced bone tissue engineering.

3.6. VAN loading, entrapment yield and release from aerogels

PBS was used as release medium to mimic the continuously renewed biological fluid (Oungeun et al., 2019). VAN release tests (Fig. 5) exhibited a two-stage profile with a 3-day sustained release (Fig. 5a,c) occurring after an initial burst release (Fig. 5b,d) for all formulations. VAN minimum inhibitory concentration (MIC) against *S. aureus* is 2.0 μg/mL (Oungeun et al., 2019), so an effective VAN concentration was maintained for all formulations from the beginning of the drug release. Thereby, aerogels provided concentrations above MIC upon implantation, potentially preventing bacterial growth over time. Similar release profiles were found for VAN-loaded nanocellulose scaffolds (Vismara et al., 2019) and chitosan-HA scaffolds (J. Zhang et al., 2012). Initial burst release was attributed to VAN release weakly adsorbed in the mesopores, while the subsequent slow VAN release was assigned to the strong interaction between the gel matrix and the VAN that retards the diffusion of the drug to the medium (Zhang et al., 2012).

VAN release profiles were similar regardless of the VAN content (Fig. 5). Interestingly, aerogels formed by alternative layers of different VAN content (MC VAN 5/15) showed a slower release than other aerogels of similar VAN content but with a homogeneous distribution of the drug (MC VAN 15). On the other hand, the comparison of the release profiles of MC nHA24 VAN10 and MC VAN10 aerogels (Fig. 5) unveiled that the presence of nHA seems to retard the VAN release from the

Table 6
VAN loading, entrapment yield and kinetic fitting parameters (k and R^2) of VAN release profiles of different aerogel formulations.

Aerogel formulation	Loading (%)	Entrapment yield (%)	k (h^{-1})	R^2
MC VAN 5	21.99 ± 0.04	74.78 ± 0.12	5.53 ± 1.25	0.90
MC VAN 10	30.71 ± 2.09	67.57 ± 4.61	4.32 ± 1.52	0.79
MC VAN 15	36.02 ± 1.55	64.84 ± 2.80	1.90 ± 0.60	0.83
MC VAN 5/15	34.77 ± 0.19	81.83 ± 0.44	2.94 ± 0.64	0.86
MC nHA 24 VAN 10	13.77 ± 4.25	63.36 ± 19.57	8.11 ± 1.25	0.92

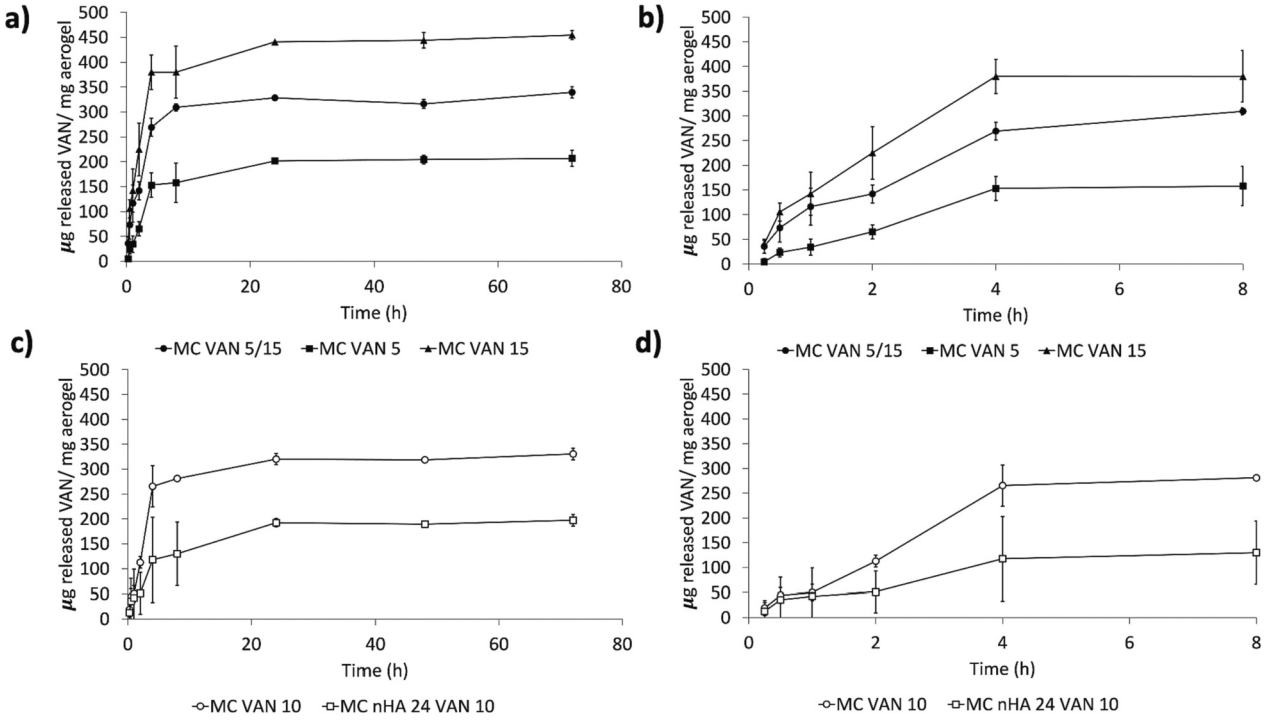

Fig. 5. VAN release profiles from different aerogel formulations in PBS pH 7.4, at 37 °C and 100 rpm for 3 days (left) and close up during the first 8 h (right).

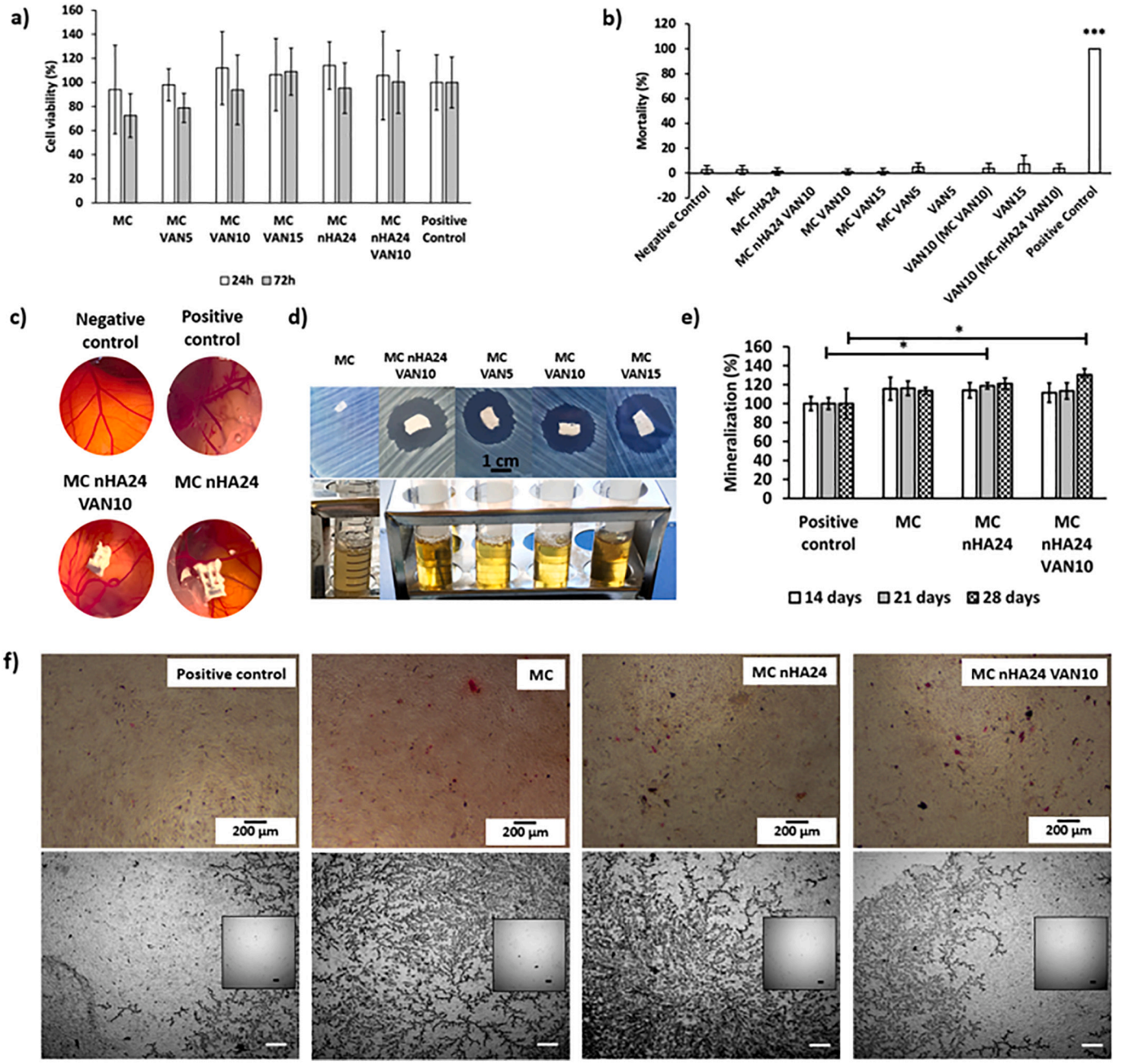

Fig. 6. Biological evaluation of 3D-printed aerogel scaffolds: (a) Cell viability tests of aerogels. Viability (expressed in %) of NIH/3T3 cells after 24 and 72 h of contact with scaffolds determined by the Resazurin cytotoxicity assay. There were no statistically significant differences among groups. (b) Mortality of *A. salina* after 24 h in contact with aerogels. Positive control: DMSO; negative control: artificial sea water. (c) HET-CAM test of aerogels. Negative control: 0.9 % (*w/v*) NaCl; positive control: 0.1 N NaOH. (d) Aerogels after 24 h of culture on TSA plates (top) and on the corresponding TSB tubes (down) seeded with *S. aureus*. (e) Mineralization values obtained after 14, 21 and 28 days for different aerogel formulations by Alizarin red staining test. (f) Optical images of MC3T3 cells in contact with aerogels after Alizarin tests (28 days) in the wet (top) and in the dry (bottom) forms (scale bar: 200 µm). Intakes: images of the same formulations after removing the dye with cetylpyridinium chloride (scale bar: 200 µm). Post hoc Tukey HSD multiple comparison tests were performed and significant differences among groups were reported as * or *** for $p < 0.05$ or $p < 0.001$, respectively.

scaffolds into the liquid medium.

High VAN entrapment yields were achieved (Table 6), indicating the suitability of the dual processing strategy to effectively load VAN in MC aerogels maybe due to the no necessity of a gelation bath in which VAN could be solubilized. All VAN release profiles fitted to the first-order pharmacokinetic model (Table 6), where the amount of drug released decreased with time and it is proportional to the amount of drug remaining in the matrix (López-Iglesias et al., 2020). VAN dissolution in PBS medium is faster than the drug release from VAN-loaded aerogels, so aerogels promoted sustained VAN release. Similar release patterns were reported for VAN-loaded chitosan aerogels (López-Iglesias et al., 2019).

3.7. Biocompatibility tests

Good biocompatibility was obtained for all formulations at different timepoints after contact with fibroblasts without statistically significant differences between aerogels and positive controls (Fig. 6a). Cell

viability results are close to previously reported ones for 3D-printed MC structures after contact with NIH/3T3 cells for 24 and 48 h (Cochis et al., 2018). Similar cytocompatibility was also reported for composite scaffolds loaded with same VAN concentrations after 24 h in contact with mesenchymal stem cells (Krishnan et al., 2020), thus suggesting that the drug released from the matrix do not present an impact on cell survival. The high cell viability obtained suggest that neither aerogel composition (MC, nHA and/or VAN, at the component contents studied) nor material processing strategies (3D-printing and $scCO_2$ drying) compromised the biocompatibility of the 3D-printed aerogels (ISO 10993-5:2009 Biological Evaluation of Medical Devices — Part 5: Tests for in Vitro Cytotoxicity, 2009).

3.8. Safety tests using A. salina model

A. salina model is employed as a method to check the safety of aerogels (Ferreira-Gonçalves et al., 2022). Statistically significant differences were found between the mortality of *A. salina* due to 24 h of contact with aerogel formulations and the positive control (DMSO) (Fig. 6b). These results confirm the safety of VAN and/or nHA-loaded aerogels and are coherent with the ones previously reported for *A. salina* in contact with the drug, being VAN extremely toxic at 10 g/L (100 % mortality of *A. salina*) and moderately toxic or non-toxic at decreasing concentrations like the herein employed (1.8–3.9 g/L) (Hernández Martínez et al., 2018).

3.9. HET-CAM assay

3D-printed aerogels were evaluated regarding their irritative potential for being used as medical devices by HET-CAM test (Coelho et al., 2019). No visual signs of hemorrhage or vascular lysis were observed after 5 min of aerogels contact with CAM, in contrast to the positive control where CAM vessels bleeding and clotting were clearly present (Fig. 6c). The same CAM structures were observed in negative controls and in CAM contacted with aerogels, suggesting the absence of impact in CAM morphology due to aerogels contact.

3.10. Antimicrobial assessment of 3D-printed aerogels

VAN-loaded aerogels were able to induce an inhibition zone in TSA plates seeded with *S. aureus* (Fig. 6d). The remarkable halos herein observed are more pronounced than the ones previously reported for other VAN-loaded scaffolds (Chen et al., 2019a; Krishnan et al., 2020; Vismara et al., 2019), maybe due to the increased contact area of aerogel formulations with TSA plates. VAN-loaded aerogels also show absence of bacterial growth in TSB tubes (Fig. 6d) confirming the high potential of these formulations as effective antimicrobial composites against *S. aureus*. Scaffolds aimed to be used as an effective treatment for bone pathologies must have dual antibacterial properties: contact bactericidal ability and drug release from the material (Fang et al., 2021). The release profile must consist on an initial rapid bactericidal ability followed by a sustained antibacterial release to prevent from infection recurrence. All VAN-loaded aerogels present contact bactericidal ability (Fig. 6d) as well as the initial and sustained antibiotic release (Fig. 5), critical for successful bone repair.

3.11. Mineralization assay

Alizarin red staining experiment was performed with relevant differences after 21 days of mineralization between the positive control (osteoblast-like cells, MC3T3 cells) and the cells in contact with MC nHA 24 aerogels (Fig. 6e). Significantly higher levels of calcium deposition ($p < 0.05$) were found for MC nHA 24 formulations thus suggesting the triggering of the mineralization process. Scaffolds with the same nHA content but also loaded with VAN (MC nHA24 VAN10) only had relevant differences in the mineralization process with respect to the controls after 28 days. This was related to a decrease in the early proliferation rate of bone marrow mesenchymal stem cells in the presence of VAN as previously reported in the 0–2000 μg/mL range, followed by an enhancement in the pre-osteoblast to osteoblast differentiation due to VAN release (Antoci et al., 2007; García-González et al., 2018; Mantripragada & Jayasuriya, 2016). Finally, scaffolds without nHA (MC in Fig. 6e) had no statistically significant influence on mineralization in comparison to the control, thus highlighting the key effect of nHA in the mineralization promotion. Moreover, bone foci observed by optical imaging were particularly dense in the aerogel formulations containing nHA (Fig. 6f), thus confirming its role in the mineralization process. Results are coherent with previous studies where different biopolymers (regenerated cellulose, chitosan) induced mineralization after 14 and 21 days in culture with MC3T3 cells when nHA was incorporated in the formulation (Maharjan et al., 2021; Ryu et al., 2020).

3.12. Sterility procedure evaluation

Sterility assurance levels (SAL 6) against bacterial endospores are required for biomaterials prior to be implanted (ISO 14937:2009 Sterilization of Health Care Products — General Requirements for Characterization of a Sterilizing Agent and the Development, Validation and Routine Control of a Sterilization Process for Medical Devices, 2009, p. 14). Different processes have been employed for medical devices sterilization but most of them are not suitable for polymeric materials as they induce changes in important features like rheological properties or stability (Ahlfeld et al., 2020). $scCO_2$ is effective for inhibiting bacterial growth arising as a green, rapid, and economic method adequate for biomaterials sterilization (Ribeiro et al., 2020; Spilimbergo et al., 2003; Sun et al., 2020). Cytoplasm and extracellular medium acidification due to CO_2 dissolution have been described as most important inactivation mechanisms of microorganisms due to the presence of $scCO_2$ (Spilimbergo et al., 2003).

No relevant changes in aerogels morphology, pore size and pore distribution were observed before (Fig. 2) and after $scCO_2$ sterilization (Fig. 7b,c,d,e). Adequate textural parameters for BTE were obtained for sterilized aerogels (Table 4), with similar values with respect to the untreated ones (Table 3). Finally, aerogels were immersed in TSB tubes and put in contact with TSA plates to evaluate the bacterial growth on $scCO_2$ sterilized aerogel structures (Fig. 7a). After 24 h of culture, TSB medium was cultured in a TSA plate for 24 h and absence of bacterial growth was observed. Sterility of biomaterials was thus confirmed by both tests.

4. Conclusions

VAN-loaded polymer-based bone scaffolds obtained by the combination of 3D-printing and aerogel technologies promise to promote bone defects repair while controlling bone infection progress in a personalized way. 3D-printed aerogels present excellent physicochemical performance (macro- and mesoporosity), high printing fidelity with respect to the original design and high drug entrapment yields, which endorse the suitability of this technological combination for the manufacturing of drug-loaded nanostructured scaffolds. Biological performances of aerogels containing nHA and/or VAN are very attractive for bone repair (high apatite mineralization appeared after bioactivity and alizarin red staining tests) and bone infection mitigation (two-stage VAN release profile providing drug therapeutic levels, and antimicrobial efficacy against *S. aureus*). *In vitro* assays in murine fibroblasts, *in vivo* tests in *A. salina* model and *in ovo* HET-CAM tests preliminarily revealed the safety of VAN-loaded aerogels. *In vivo* efficacy of the VAN-loaded aerogel scaffolds in bone infection treatments need to be evaluated. Sterilization of 3D-printed aerogels using $scCO_2$ as sterilant agent turn out to be very adequate, as it resulted in minor physicochemical changes of scaffolds. Furthermore, no relevant textural changes were observed in the scaffolds after 7 months of storage under mild conditions. Finally,

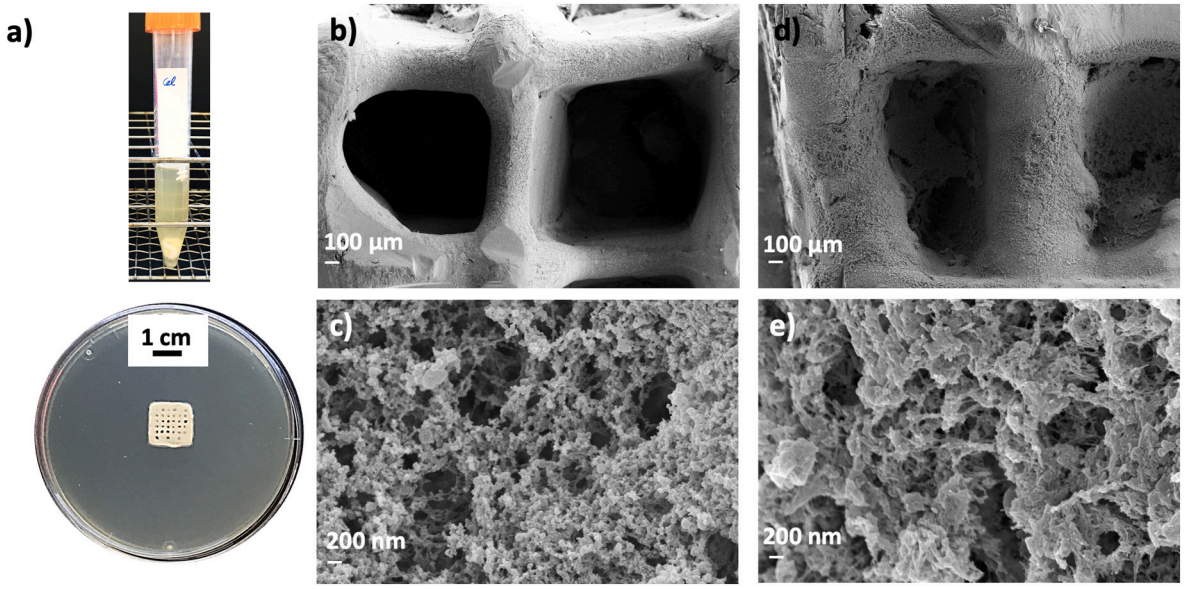

Fig. 7. (a) Microbiological tests of sterilized MC nHA24 aerogels seeded on TSB tubes (top) and on TSA plates (down) after 24 h of culture. No microbial growth was observed in none of the tested cases. SEM images of sterilized aerogels: (b,c) MC, and (d,e) MC nHA 24.

the absence of a negative impact in the microstructure due to the customization of the drug content distribution within the aerogels offer new personalized applications, e.g., scaffolds with patient specific external dimensions fitting the defect and with tailored gradient drug concentration profiles to optimize the long-term performance of aerogels.

CRediT authorship contribution statement

All authors have substantially contributed to this manuscript and agreed on this submission.

Declaration of competing interest

The authors declare that they have no known competing financial interests or personal relationships that could have appeared to influence the work reported in this paper.

Data availability

Data will be made available on request.

Acknowledgments

This work was supported by MICINN [PID2020-120010RB-I00/AEI/10.13039/501100011033; PDC2022-133526-I00/AEI/10.13039/501100011033], Xunta de Galicia [ED431C 2020/17], Agencia Estatal de Investigación [AEI] and FEDER funds. Work carried out in the framework of the COST Action CA18125 “Advanced Engineering and Research of aeroGels for Environment and Life Sciences” (AERoGELS) and funded by the European Commission. A.I.-M. acknowledges to Xunta de Galicia [ED481A-2020/104] and T.F.-G. to Fundação para a Ciência e a Tecnologia (FCT) [SFRH/BD/147306/2019] for their predoctoral research fellowships.

Appendix A. Supplementary data

Supplementary data to this article can be found online at https://doi.org/10.1016/j.carbpol.2023.121536.

References

Ahlfeld, T., Guduric, V., Duin, S., Akkineni, A. R., Schütz, K., Kilian, D., … Gelinsky, M. (2020). Methylcellulose – A versatile printing material that enables biofabrication of tissue equivalents with high shape fidelity. *Biomaterials Science, 8*(8), 2102–2110. https://doi.org/10.1039/D0BM00027B

Antoci, V., Adams, C. S., Hickok, N. J., Shapiro, I. M., & Parvizi, J. (2007). Antibiotics for local delivery systems cause skeletal cell toxicity in vitro. *Clinical Orthopaedics & Related Research, 462*, 200–206. https://doi.org/10.1097/BLO.0b013e31811ff866

Barakat, A., Schilling, W. H. K., Sharma, S., Guryel, E., & Freeman, R. (2019). Chronic osteomyelitis: A review on current concepts and trends in treatment. *Orthopaedics and Traumatology, 33*(3), 181–187. https://doi.org/10.1016/j.mporth.2019.03.005

Bernardes, B. G., Del Gaudio, P., Alves, P., Costa, R., García-Gonzaléz, C. A., & Oliveira, A. L. (2021). Bioaerogels: Promising nanostructured materials in fluid management, healing and regeneration of wounds. *Molecules, 26*(13), 3834. https://doi.org/10.3390/molecules26133834

Buechner, P. M., & Lakes, R. S. (2003). Size effects in the elasticity and viscoelasticity of bone. *Biomechanics and Modeling in Mechanobiology, 1*(4), 295–301. https://doi.org/10.1007/s10237-002-0026-8

Chen, X., Gao, C., Jiang, J., Wu, Y., Zhu, P., & Chen, G. (2019a). 3D printed porous PLA/nHA composite scaffolds with enhanced osteogenesis and osteoconductivity *in vivo* for bone regeneration. *Biomedical Materials, 14*(6), Article 065003. https://doi.org/10.1088/1748-605X/ab388d

Chen, S., Shi, Y., Zhang, X., & Ma, J. (2019b). 3D printed hydroxyapatite composite scaffolds with enhanced mechanical properties. *Ceramics International, 45*(8), 10991–10996. https://doi.org/10.1016/j.ceramint.2019.02.182

Chen, Z.-J., Shi, H.-H., Zheng, L., Zhang, H., Cha, Y.-Y., Ruan, H.-X., Zhang, Y., & Zhang, X.-C. (2021). A new cancellous bone material of silk fibroin/cellulose dual network composite aerogel reinforced by nano-hydroxyapatite filler. *International Journal of Biological Macromolecules, 182*, 286–297. https://doi.org/10.1016/j.ijbiomac.2021.03.204

Cochis, A., Bonetti, L., Sorrentino, R., Contessi Negrini, N., Grassi, F., Leigheb, M., … Farè, S. (2018). 3D printing of thermo-responsive methylcellulose hydrogels for cell-sheet engineering. *Materials, 11*(4), 579. https://doi.org/10.3390/ma11040579

Coelho, C. C., Grenho, L., Gomes, P. S., Quadros, P. A., & Fernandes, M. H. (2019). Nano-hydroxyapatite in oral care cosmetics: Characterization and cytotoxicity assessment. *Scientific Reports, 9*(1), 11050. https://doi.org/10.1038/s41598-019-47491-z

Corker, A., Ng, H. C.-H., Poole, R. J., & García-Tuñón, E. (2019). 3D printing with 2D colloids: Designing rheology protocols to predict ‘printability’ of soft-materials. *Soft Matter, 15*(6), 1444–1456. https://doi.org/10.1039/C8SM01936C

Derakhshanfar, S., Mbeleck, R., Xu, K., Zhang, X., Zhong, W., & Xing, M. (2018). 3D bioprinting for biomedical devices and tissue engineering: A review of recent trends and advances. *Bioactive Materials, 3*(2), 144–156. https://doi.org/10.1016/j.bioactmat.2017.11.008

Drouet, C. (2013). Apatite formation: Why it may not work as planned, and how to conclusively identify apatite compounds. *BioMed Research International, 2013*, 1–12. https://doi.org/10.1155/2013/490946

Duarte, A. R. C., Caridade, S. G., Mano, J. F., & Reis, R. L. (2009). Processing of novel bioactive polymeric matrixes for tissue engineering using supercritical fluid technology. *Materials Science and Engineering: C, 29*(7), Article 7. https://doi.org/10.1016/j.msec.2009.04.012

Fang, B., Qiu, P., Xia, C., Cai, D., Zhao, C., Chen, Y., Wang, H., Liu, S., Cheng, H., Tang, Z., Wang, B., Fan, S., & Lin, X. (2021). Extracellular matrix scaffold crosslinked with vancomycin for multifunctional antibacterial bone infection therapy. *Biomaterials, 268*, Article 120603. https://doi.org/10.1016/j.biomaterials.2020.120603

Ferreira-Gonçalves, T., Iglesias-Mejuto, A., Linhares, T., Coelho, J. M. P., Vieira, P., Faísca, P., … Reis, C. P. (2022). Biological thermal performance of organic and inorganic aerogels as patches for photothermal therapy. *Gels, 8*(8), 485. https://doi.org/10.3390/gels8080485

Gallarate, M., Chirio, D., Chindamo, G., Peira, E., & Sapino, S. (2021). Osteomyelitis: Focus on conventional treatments and innovative drug delivery systems. *Current Drug Delivery, 18*(5), 532–545. https://doi.org/10.2174/1567201817666200915093224

García-González, C. A., Barros, J., Rey-Rico, A., Redondo, P., Gómez-Amoza, J. L., Concheiro, A., … Monteiro, F. J. (2018). Antimicrobial properties and osteogenicity of vancomycin-loaded synthetic scaffolds obtained by supercritical foaming. *ACS Applied Materials & Interfaces, 10*(4), Article 4. https://doi.org/10.1021/acsami.7b17375

García-González, C. A., Sosnik, A., Kalmár, J., De Marco, I., Erkey, C., Concheiro, A., & Alvarez-Lorenzo, C. (2021). Aerogels in drug delivery: From design to application. *Journal of Controlled Release, 332*, 40–63. https://doi.org/10.1016/j.jconrel.2021.02.012

Giuseppe, M. D., Law, N., Webb, B., Macrae, R., A., Liew, L. J., Sercombe, T. B., … Doyle, B. J. (2018). Mechanical behaviour of alginate-gelatin hydrogels for 3D bioprinting. *Journal of the Mechanical Behavior of Biomedical Materials, 79*, 150–157. https://doi.org/10.1016/j.jmbbm.2017.12.018

Hamidi, M., R., Jovanova, B., & Kadifkova Panovska, T. (2014). Toxicological evaluation of the plant products using brine shrimp (Artemia salina L.) model. *Macedonian. Pharmaceutical Bulletin, 60*(01), 9–18. https://doi.org/10.33320/maced.pharm.bull.2014.60.01.002

Hernández Martínez, E. M., Carrazana García, D. I., González González, R., García López, A., Marrero Chang, O., Águila Jiménez, E., … López Hernández, Y. (2018). Ecotoxicidad aguda en Physa cubensis P. y Artemia salina L. de 8 antibacterianos con riesgo ambiental. *Revista de Toxicología, 34*(2), 118–123.

Iglesias-Mejuto, A., & García-González, C. A. (2021). 3D-printed alginate-hydroxyapatite aerogel scaffolds for bone tissue engineering. *Materials Science and Engineering: C, 131*, Article 112525. https://doi.org/10.1016/j.msec.2021.112525

Iglesias-Mejuto, A., & García-González, C. A. (2022). 3D-printed, dual crosslinked and sterile aerogel scaffolds for bone tissue engineering. *Polymers, 14*(6), 1211. https://doi.org/10.3390/polym14061211

ISO 10993-5:2009 Biological evaluation of medical devices—Part 5: Tests for in vitro cytotoxicity. (2009). *ISO/TC 194 Biological and clinical evaluation of medical devices*.

ISO 14937:2009 Sterilization of health care products—General requirements for characterization of a sterilizing agent and the development, validation and routine control of a sterilization process for medical devices. (2009). *ISO/TC 198 Sterilization of health care products*.

Jiang, W., Mei, H., & Zhao, S. (2021). Applications of 3D bio-printing in tissue engineering and biomedicine. *Journal of Biomedical Nanotechnology, 17*(6), 989–1006. https://doi.org/10.1166/jbn.2021.3078

Kohyama, K., Morishima, Y., Arisawa, K., Arisawa, Y., & Kato, H. (2018). Immediate and long-term results of unsintered hydroxyapatite and poly L-lactide composite sheets for orbital wall fracture reconstruction. *Journal of Plastic, Reconstructive & Aesthetic Surgery, 71*(7), 1069–1075. https://doi.org/10.1016/j.bjps.2018.03.006

Kokubo, T., & Takadama, H. (2006). How useful is SBF in predicting in vivo bone bioactivity? *Biomaterials, 27*(15), Article 15. https://doi.org/10.1016/j.biomaterials.2006.01.017

Krishnan, A. G., Biswas, R., Menon, D., & Nair, M. B. (2020). Biodegradable nanocomposite fibrous scaffold mediated local delivery of vancomycin for the treatment of MRSA infected experimental osteomyelitis. *Biomaterials Science, 8*(9), 2653–2665. https://doi.org/10.1039/D0BM00140F

Kumar, A., Negi, Y. S., Choudhary, V., & Bhardwaj, N. K. (2014). Microstructural and mechanical properties of porous biocomposite scaffolds based on polyvinyl alcohol, nano-hydroxyapatite and cellulose nanocrystals. *Cellulose, 21*(5), 3409–3426. https://doi.org/10.1007/s10570-014-0339-7

Lin, R., Li, A., Lu, L., & Cao, Y. (2015). Preparation of bulk sodium carboxymethyl cellulose aerogels with tunable morphology. *Carbohydrate Polymers, 118*, 126–132. https://doi.org/10.1016/j.carbpol.2014.10.075

López-Iglesias, C., Barros, J., Ardao, I., Monteiro, F. J., Alvarez-Lorenzo, C., Gómez-Amoza, J. L., & García-González, C. A. (2019). Vancomycin-loaded chitosan aerogel particles for chronic wound applications. *Carbohydrate Polymers, 204*, 223–231. https://doi.org/10.1016/j.carbpol.2018.10.012

López-Iglesias, C., Quílez, C., Barros, J., Velasco, D., Alvarez-Lorenzo, C., Jorcano, J. L., … García-González, C. A. (2020). Lidocaine-loaded solid lipid microparticles (SLMPs) produced from gas-saturated solutions for wound applications. *Pharmaceutics, 12*(9), 870. https://doi.org/10.3390/pharmaceutics12090870

Lv, X.-F., Zhou, D.-M., Sun, X.-H., & Zhao, Z. (2022). Nano sized hydroxyapatite-polylactic acid-vancomycin in alleviation of chronic osteomyelitis. *Drug Design, Development and Therapy, 16*, 1983–1993. https://doi.org/10.2147/DDDT.S356257

Maharjan, B., Park, J., Kaliannagounder, V. K., Awasthi, G. P., Joshi, M. K., Park, C. H., & Kim, C. S. (2021). Regenerated cellulose nanofiber reinforced chitosan hydrogel scaffolds for bone tissue engineering. *Carbohydrate Polymers, 251*, Article 117023. https://doi.org/10.1016/j.carbpol.2020.117023

Mantripragada, V. P., & Jayasuriya, A. C. (2016). Effect of dual delivery of antibiotics (vancomycin and cefazolin) and BMP-7 from chitosan microparticles on Staphylococcus epidermidis and pre-osteoblasts in vitro. *Materials Science and Engineering: C, 67*, 409–417. https://doi.org/10.1016/j.msec.2016.05.033

Ng, P., Pinho, A. R., Gomes, M. C., Demidov, Y., Krakor, E., Grume, D., … Maleki, H. (2022). Fabrication of antibacterial, osteo-inductor 3D printed aerogel-based scaffolds by incorporation of drug laden hollow mesoporous silica microparticles into the self-assembled silk fibroin biopolymer. *Macromolecular Bioscience, 22*(4), 2100442. https://doi.org/10.1002/mabi.202100442

Oungeun, P., Rojanathanes, R., Pinsornsak, P., & Wanichwecharungruang, S. (2019). Sustaining antibiotic release from a poly(methyl methacrylate) bone-spacer. *ACS Omega, 4*(12), 14860–14867. https://doi.org/10.1021/acsomega.9b01472

Panraksa, P., Udomsom, S., Rachtanapun, P., Chittasupho, C., Ruksiriwanich, W., & Jantrawut, P. (2020). Hydroxypropyl methylcellulose E15: A hydrophilic polymer for fabrication of orodispersible film using syringe extrusion 3D printer. *Polymers, 12*(11), 2666. https://doi.org/10.3390/polym12112666

Poeppl, W., Lingscheid, T., Bernitzky, D., Schwarze, U. Y., Donath, O., Perkmann, T., … Burgmann, H. (2014). Efficacy of fosfomycin compared to vancomycin in treatment of implant-associated chronic methicillin-resistant staphylococcus aureus osteomyelitis in rats. *Antimicrobial Agents and Chemotherapy, 58*(9), 5111–5116. https://doi.org/10.1128/AAC.02720-13

Recommended Test Method Protocol: Hen''s Egg Test – Chorioallantoic Membrane (HET-CAM) Test Method. (2010). *ICCVAM*.

Ribeiro, N., Soares, G. C., Santos-Rosales, V., Concheiro, A., Alvarez-Lorenzo, C., García-González, C. A., & Oliveira, A. L. (2020). A new era for sterilization based on supercritical CO_2 technology. *Journal of Biomedical Materials Research Part B: Applied Biomaterials, 108*(2), 399–428. https://doi.org/10.1002/jbm.b.34398

Ryu, J.-H., Kang, T.-Y., Shin, H., Kim, K.-M., Hong, M.-H., & Kwon, J.-S. (2020). Osteogenic properties of novel methylsulfonylmethane-coated hydroxyapatite scaffold. *International Journal of Molecular Sciences, 21*(22), 8501. https://doi.org/10.3390/ijms21228501

Salerno, A., Diéguez, S., Diaz-Gomez, L., Gómez-Amoza, J. L., Magariños, B., Concheiro, A., … García-González, C. A. (2017). Synthetic scaffolds with full pore interconnectivity for bone regeneration prepared by supercritical foaming using advanced biofunctional plasticizers. *Biofabrication, 9*(3), Article 035002. https://doi.org/10.1088/1758-5090/aa78c5

Shin, J. Y., Yeo, Y. H., Jeong, J. E., Park, S. A., & Park, W. H. (2020). Dual-crosslinked methylcellulose hydrogels for 3D bioprinting applications. *Carbohydrate Polymers, 238*, Article 116192. https://doi.org/10.1016/j.carbpol.2020.116192

Spellberg, B., & Lipsky, B. A. (2012). Systemic antibiotic therapy for chronic osteomyelitis in adults. *Clinical Infectious Diseases, 54*(3), 393–407. https://doi.org/10.1093/cid/cir842

Spilimbergo, S., Dehghani, F., Bertucco, A., & Foster, N. R. (2003). Inactivation of bacteria and spores by pulse electric field and high pressure CO2 at low temperature. *Biotechnology and Bioengineering, 82*(1), 118–125. https://doi.org/10.1002/bit.10554

Sun, Y., Lovric, V., Wang, T., Oliver, R. A., & Walsh, W. R. (2020). Effects of SCCO2, gamma irradiation, and sodium dodecyl sulfate treatments on the initial properties of tendon allografts. *International Journal of Molecular Sciences, 21*(5), 1565. https://doi.org/10.3390/ijms21051565

Tetik, H., Wang, Y., Sun, X., Cao, D., Shah, N., Zhu, H., … Lin, D. (2021). Additive manufacturing of 3D aerogels and porous scaffolds: A review. *Advanced Functional Materials, 31*(45), 2103410. https://doi.org/10.1002/adfm.202103410

Tohamy, K. M., Mabrouk, M., Soliman, I. E., Beherei, H. H., & Aboelnasr, M. A. (2018). Novel alginate/hydroxyethyl cellulose/hydroxyapatite composite scaffold for bone regeneration: In vitro cell viability and proliferation of human mesenchymal stem cells. *International Journal of Biological Macromolecules, 112*, 448–460. https://doi.org/10.1016/j.ijbiomac.2018.01.181

Tohamy, K. M., Soliman, I. E., Mabrouk, M., ElShebiney, S., Beherei, H. H., Aboelnasr, M. A., & Das, D. B. (2018). Novel polysaccharide hybrid scaffold loaded with hydroxyapatite: Fabrication, bioactivity, and in vivo study. *Materials Science and Engineering: C, 93*, 1–11. https://doi.org/10.1016/j.msec.2018.07.054

Trakulsujaritchok, T., & Hourston, D. J. (2006). Damping characteristics and mechanical properties of silica filled PUR/PEMA simultaneous interpenetrating polymer networks. *European Polymer Journal, 42*(11), 2968–2976. https://doi.org/10.1016/j.eurpolymj.2006.07.028

Trampuz, A., & Zimmerli, W. (2008). Diagnosis and treatment of implant-associated septic arthritis and osteomyelitis. *Current Infectious Disease Reports, 10*(5), 394–403. https://doi.org/10.1007/s11908-008-0064-1

Valarmathi, N., & Sumathi, S. (2022). Zinc substituted hydroxyapatite/silk fiber/methylcellulose nanocomposite for bone tissue engineering applications. *International Journal of Biological Macromolecules, 214*, 324–337. https://doi.org/10.1016/j.ijbiomac.2022.06.033

Vismara, E., Bernardi, A., Bongio, C., Farè, S., Pappalardo, S., Serafini, A., … Torri, G. (2019). Bacterial nanocellulose and its surface modification by glycidyl methacrylate and ethylene glycol dimethacrylate. Incorporation of vancomycin and ciprofloxacin. *Nanomaterials (Basel, Switzerland), 9*(12), Article E1668. https://doi.org/10.3390/nano9121668

Wang, Z., Zhu, W., Huang, R., Zhang, Y., Jia, C., Zhao, H., … Xue, Y. (2020). Fabrication and characterization of cellulose nanofiber aerogels prepared via two different drying techniques. *Polymers, 12*(11), 2583. https://doi.org/10.3390/polym12112583

Yahya, E. B., Amirul, A. A., H. P. S., A. K., Olaiya, N. G., Iqbal, M. O., … Adnan, A. S. (2021). Insights into the role of biopolymer aerogel scaffolds in tissue engineering

and regenerative medicine. *Polymers, 13*(10), 1612. https://doi.org/10.3390/polym13101612

Zhang, J., Wang, C., Wang, J., Qu, Y., & Liu, G. (2012). *In vivo* drug release and antibacterial properties of vancomycin loaded hydroxyapatite/chitosan composite. *Drug Delivery, 19*(5), 264–269. https://doi.org/10.3109/10717544.2012.704093

Zhang, M., Jiang, S., Han, F., Li, M., Wang, N., & Liu, L. (2021). Anisotropic cellulose nanofiber/chitosan aerogel with thermal management and oil absorption properties. *Carbohydrate Polymers, 264*, Article 118033. https://doi.org/10.1016/j.carbpol.2021.118033